Improving the strength-ductility balance of medium-Mn Q&P steel by controlling cold-worked ferrite microstructure

Li, Jiayu; Xu, Yunbo; Jing, Yi; Gao, Yijing; Liu, Hongliang; Yu, Yongmei; Banis, Alexandros; Kestens, Leo A.I.; Petrov, Roumen H.

DOI
10.1016/j.matchar.2023.113377

Publication date
2023

Document Version
Final published version

Published in
Materials Characterization

Materials Characterization 205 (2023) 113377

Contents lists available at ScienceDirect

Materials Characterization

journal homepage: www.elsevier.com/locate/matchar

Improving the strength-ductility balance of medium-Mn Q&P steel by controlling cold-worked ferrite microstructure

Jiayu Li [a,d], Yunbo Xu [a,*], Yi Jing [a], Yijing Gao [a], Hongliang Liu [b], Yongmei Yu [c,*], Alexandros Banis [d], Leo A.I. Kestens [d,e], Roumen H. Petrov [d,e]

[a] State Key Laboratory of Rolling Technology and Automation, Northeastern University, Shenyang 110819, China
[b] Technology Research Institute of Bengang Steel Plates Co. Ltd., Benxi 117000, China
[c] School of Mechanical and Power Engineering, Shenyang University of Chemical Technology, Shenyang 110142, China
[d] Department of Electromechanical, Systems & Metal Engineering, Ghent University, Technologiepark 903, 9052 Gent, Belgium
[e] Delft University of Technology, Department of Materials Science and Engineering, Mekelweg 2, 2628CD Delft, the Netherlands

ARTICLE INFO

Keywords:
Cold-worked ferrite
Medium-manganese steel
Quenching and partitioning process
Austenitization kinetics
Microstructure and mechanical properties

ABSTRACT

The phase transformations, microstructure and properties of two Medium-Mn processed via quenching and partitioning steels were compared in this contribution and a new strategy for controlling mechanical properties by introducing and controlling cold-worked ferrite prior to heat treatment is proposed. It was found that during heating, the recovery and recrystallization of cold-worked ferrite compete with austenitization, thereby inhibiting the coarsening of austenite. The cold-worked ferrite interface will significantly delay the austenitization kinetics during the partitioning local equilibrium stage compared to martensite. These results lead to a diverse parent austenite, as well as a refined martensite substructure. As a result, the randomly distributed variants increase the number of effective grain boundaries, thus enhancing yield strength. The intercritical annealing process at a temperature of 860 °C resulted in the formation of fresh martensite-retained austenite (M/RA) constituents exhibiting a remarkably fine (<2 μm) and uniform grain morphology. Such microstructure yielded substantial improvement in both the strength and ductility of the steel. The proposed treatment led to excellent elongation (24%) at fracture, combined with very high ultimate tensile strength and yield strength of 1345 MPa and 1163 MPa, respectively, of the steel, resulting in a product of strength and elongation that exceed 32 GPa%.

1. Introduction

Advanced high-strength steels (AHSS) are widely used in automotive manufacturing owing to their excellent combination of high strength and toughness that contribute to safety and energy savings [1–3]. Medium-Mn steel (3–12 wt% Mn) and Quenching and Partitioning (Q&P) steel have become attractive third-generation AHSS because of their excellent strength-ductility balance [1,4–6]. By optimizing the chemical composition, annealing process and microstructure, Medium-Mn steel can exhibit an astonishing product of strength and elongation (PSE), above 30 GPa% [6–12]. However, it has been reported that low-carbon (C < 0.2 wt%) medium-Mn steel has achieved excellent elongation, but the material has relatively low strength (ultimate tensile strength, UTS < 1000 MPa; yield strength, YS < 850 MPa), limiting its effectiveness in intrusion resistance during vehicular collisions [5,7,11–14]. Another disadvantage of this steel is that it often exhibits discontinuous yielding and serration behavior that can seriously deteriorate surface quality during forming [15]. More importantly, prolonged annealing of the material is required due to the low diffusivity of Mn [11–14]; hence adapting this system to industrial production is challenging. Different from medium-Mn steel, which stabilize austenite with the use of Mn atoms, Q&P steel achieves stabilization of austenite by partitioning carbon atoms [16–18]. Many fruitful studies on low-carbon Q&P steels have been reported [19–22]. However, the strength-ductility combination of conventional low-carbon Q&P steels is mediocre, usually achieving a PSE value of <25 GPa% [23,24]. This is especially true for high YS/UTS ratio Q&P steels, which often require additional alloying elements and complex heat treatment processes [25–28], thereby hindering the application of such steels.

Many studies have shown that applying the Q&P process to medium-Mn steel can improve the material's mechanical properties. De Moor et al. [23] pioneered the study of medium-Mn Q&P steel in the C-Si-Mn

* Corresponding authors.
E-mail addresses: yunbo_xu@126.com (Y. Xu), yongmei_yu@126.com (Y. Yu).

https://doi.org/10.1016/j.matchar.2023.113377
Received 5 July 2023; Received in revised form 20 September 2023; Accepted 5 October 2023
Available online 9 October 2023

system, and the high YS/UTS values attracted great attention. De Cooman et al. [29] experimented on V-containing medium-Mn steel. The experiments highlighted the key advantage of this type of Q&P steel is the elimination of discontinuous yielding and serration behavior. Cho et al. [30]. reported that under appropriate annealing parameters, medium-Mn Q&P steel has excellent potential to obtain ultrahigh strength (UTS > 1600 MPa) by simultaneously utilizing transformation-induced plasticity (TRIP) and twining induced plasticity (TWIP) effects. In order to improve the surface quality and machinability of steel sheets [31,32], in recent years, researchers have explored the development of medium-Mn Q&P steel by replacing Si with Al. Kim et al. [33] applied the Q&P process to 0.2C-10Mn-2Al steel, revealing that the alloy can effectively retain austenite even at low partitioning temperature (200 °C). Wu et al. [34] loaded a certain pre-strain on Al-added medium-Mn Q&P steel. They showed that the ductility can be further improved, which may be related to the heterogeneous multi-phase microstructure. On the contrary, Kaar et al. [35] believed that Al reduces the retention capacity of retained austenite (RA), resulting in mediocre mechanical properties attributed to the appearance of bainite. From the above studies, it can be seen that the addition of Al induces microstructural complexity, resulting in inconsistent experimental observations and interpretations, with some results even contradicting each other. Therefore, it is necessary to investigate further and clarify the effect of microstructure on medium-Mn Q&P steel.

Studies have shown that by adding Al or to reducing the cold rolling force, ferrite components will likely be introduced during the smelting and processing of medium-Mn steel [6,15,33–37]. It has been reported that the heating process in low-carbon steel is accompanied by phenomena such as ferrite or martensite recovery and recrystallization, which could compete and interfere with the austenite nucleation [38,39]. This complex coupling phenomenon has been shown to potentially impact the mechanical properties in conventional low carbon steel [40,41]. In addition, Suh's investigations showed that promoting ferrite recrystallization in medium-Mn TRIP steel is a potential way to refine austenite grain and improve mechanical properties [37]. Nevertheless, the initial microstructure containing cold-worked ferrite is considered a commonplace phenomenon in cold-rolled strips, and its influence on the subsequent microstructure evolution and mechanical properties of medium-Mn Q&P steel has been almost neglected and rarely studied. The results related to conventional low-carbon steel are not applicable due to differences in composition and microstructure. Therefore, conducting an in-depth investigation of this complex coupling effect in medium-Mn Q&P steel is worthwhile.

In this contribution, compared with the common composition system of C-Si-Mn, adding 1 wt% Al led to a significant expansion of the temperature range where ferrite exists, successfully preserving the cold-worked ferrite. As a result, a medium-Mn Q&P steel with extremely high strength (1264 MPa–1522 MPa) and a PSE ranging from 22 GPa% to 32 GPa% is successfully developed due to retardation of austenite formation kinetics and microstructure refinement by cold-worked ferrite.

2. Experimental procedures

Two series of medium-Mn steels were carefully designed to study the influence of cold-work ferritic (Table 1). Steel A (0.2C-5.05Mn-1.56Si) is Al-free, and based on this fact, an Al-added steel (0.2C-5.09Mn-1.01Al-1.12Si) was designed. Considering that high C and Mn contents will deteriorate weldability and increase the difficulty of smelting, the weight percentages of C and Mn were controlled at about 0.2 wt% and 5 wt%, respectively. The designed steels were melted in a vacuum furnace and subsequently hot forged into slabs with cross-sectional dimensions of 100 × 80 mm. As shown in Fig. 1, these slabs were then heated to 1200 °C and homogenized for 4 h. Afterward, the slabs were subjected to hot rolling at finish rolling temperatures of ~880 °C–900 °C to obtain thickness of 4 mm. According to our previous study [42], in order to introduce the same volume fraction of ferrite in advance (~50%), the hot-rolled strips of steel A and steel B were subjected to annealing at 660 °C and 670 °C for 3 h and 2 h, respectively. After pickling with hydrochloric acid, the hot-rolled sheets were then multi-step cold-rolled to a final thickness of 1.2 mm. Tensile samples (gauge length: 25 mm and width: 12.5 mm) were cut along the rolling direction from the cold-rolled sheet. The austenite formation start (Ac_1, 608 °C and 640 °C) and completed (Ac_3, 830 °C and 902 °C) temperatures of as-produced steels A and B were determined using Bahr DIL 805 A/D dilatometry.

Table 1
Chemical compositions of the steels used (weight percent, wt%).

Steel	C	Mn	Si	Al
Reference steel A	0.2	5.05	1.56	0
Al-added steel B	0.2	5.09	1.12	1.01

The Q&P samples were annealed for 300 s at different temperatures (840/860/880/900 °C) in a tube resistance furnace filled with nitrogen. In order to obtain sufficient tempered martensite to ensure the effect of carbon partitioning, according to the calculation of the classic constrained carbon equilibrium (CCE) model [16–18], the samples were then initially quenched to 150 °C to obtain the maximum volume fraction of RA. Samples were intentionally kept for 30 s in a salt bath to eliminate the temperature gradient. The specimens were then reheated to 450 °C for 300 s for C partitioning and then water quenched. For convenience, the Q&P samples of the two steels are referred to as A(B)-840/860/880/900, respectively. To characterize the degree of ferrite recrystallization and austenitization, interrupted quenching (IQ) tests were designed. These tests involved holding the cold-rolled specimens at different temperatures using a Bahr DIL-805 dilatometer. The dilatometer specimens with the dimension of 10 × 4 × 1.5 mm were used. For the interrupted quenching tests, the specimens were first annealed at 650/750/840 °C for non-isothermal, and immediately quenched to ambient temperature, hereafter referred to as A(B)-IQ-1/2/3, respectively. The mechanical properties were tested using an Instron-5569 tensile machine operated at an ambient temperature of 20 °C with a speed of 0.05 mm/s. The samples were observed using the FEI Quanta™ 450-FEG SEM. In addition, Electron backscatter diffraction (EBSD) was used to analyze representative samples. Due to the martensitic microstructure, careful sample preparation was essential to improve the quality of the obtained Kikuchi patterns. After conventional mechanical grinding, samples were polished using 3 μm and 1 μm Struers suspension for 20 min, respectively, followed by 0.04 μm colloidal silica (Struers OPU suspension) for 3 min and rinsed quickly with ethanol. The EBSD scans were performed at 20 kV and 2.7 nA on a square scan grid, with a step size of 0.05 μm. Post-processing of the EBSD data was generated by commercial OIM-TSL software version 8.6 with a confidence index (CI) value >0.1. In addition, transmission electron microscopy (TEM) samples were prepared by a twin-jet polisher (operating voltage: 32 V) in a 10 vol% perchlorate ethanol solution at −25 °C. The RA fraction was detected by X-ray diffraction (XRD) using Cu-Kα radiation. The samples were scanned over 2Theta range from 40° to 120° with a scanning rate of 0.03°/s. Before the XRD characterization, all samples were sequentially polished by using the 3 μm, 1 μm and OPU of Struers suspension. The volume fraction of RA (V_γ) was obtained using the integrated intensity of (200), (211) BCC peaks and (200), (220), and (311) FCC peaks. Additionally, the element content and distribution of each constituent phase were calculated under ortho-equilibrium and local equilibrium conditions using the Thermo-Calc software (databases: TCFE9, MOBFE4).

3. Results

3.1. Characterization of the initial microstructure

Previous studies of these steels by our research group have shown that after the intercritical annealing (IA) process, the microstructures of

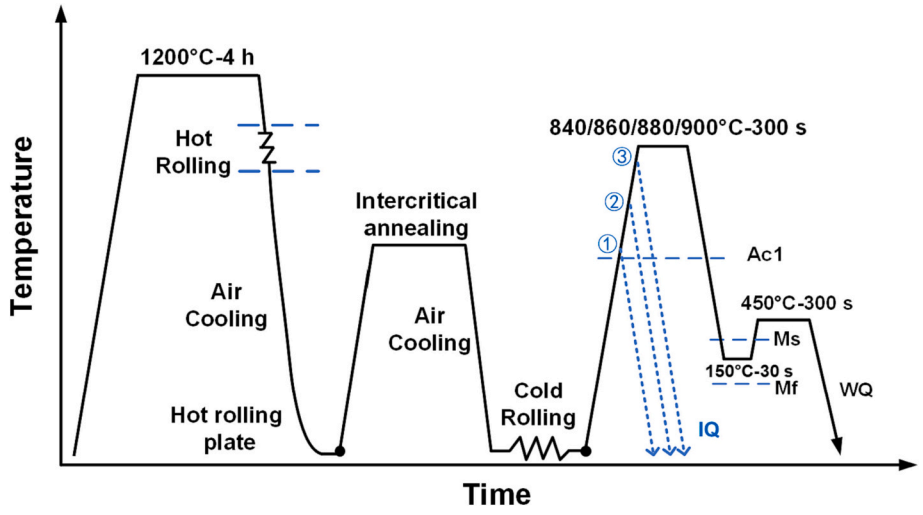

Fig. 1. Schematic of the heat treatment involved: intercritical annealing was used before cold working to prefabricate a 50% volume fraction of ferrite in both steels. A_{c1} indicates austenite formation start temperature; Ms. and M_f are abbreviations for martensite start temperature and finish temperature, respectively; the blue lines represent the interrupted quenching (IQ) process, where 1, 2, and 3 correspond to the peak temperatures 650/750/840 °C, respectively; WQ, water-quenching. In order to simulate the actual experiment and avoid the phase transition during cooling stage, the heating rate and cooling rate for all dilatometer experiments were 10 °C/s and 40 °C/s, respectively. (For interpretation of the references to colour in this figure legend, the reader is referred to the web version of this article.)

hot-rolled sheets are very similar, with the contents of ferrite (F) of ~50 vol% and RA of ~50 vol% in both steels correspond closely to the calculated equilibrium fractions [42]. Fig. 2 shows the EBSD maps after cold rolling, i.e., the initial microstructure before the Q&P process. Image quality (IQ) maps can adequately reveal different microstructures. The higher the IQ value, the lighter the colour of the corresponding area, indicating less lattice distortion and defects inside the grains [43]. Notably, EBSD and XRD measurements have shown that RA disappears after cold rolling of these steels. Therefore, before the Q&P process, the microstructure contains severely deformed intercritical ferrite, and the martensite produced by strain-induced martensite transformation (SIMT) of RA, which undergoes deformation during cold rolling. For convenience, the martensite produced by SIMT is referred to as SM. The darkest areas in Fig. 2a and b correspond to SM due to the low quality of Kikuchi patterns. Similar to SM, intercritical ferrite undergoes severe plastic deformation during cold rolling, forming a band-like morphology. This cold-worked ferrite will be deliberately retained for participation in the subsequent heating process, and is referred to as CF hereinafter. Furthermore, shear bands located at ~25° with respect to the RD are observed in both steels and the SM is situated preferably there.

3.2. Characterization of microstructure morphology of Q&P samples

Figure 3 reveals the microstructures of steels with different austenitization histories but with the same Q&P final treatment. A marked difference is noted between steels A and B. The microstructure of steel A remains virtually unchanged with different austenitization temperatures. The microstructure is mainly composed of lath-like RA and tempered martensite (TM), formed during the initial quenching step. Fine carbides resulting from martensite tempering are observed inside the TM. The fresh martensite (M) and RA are mixed to form martensite-retained austenite (abbreviated as M/RA) islands.

In contrast to steel A, the microstructure of steel B changes

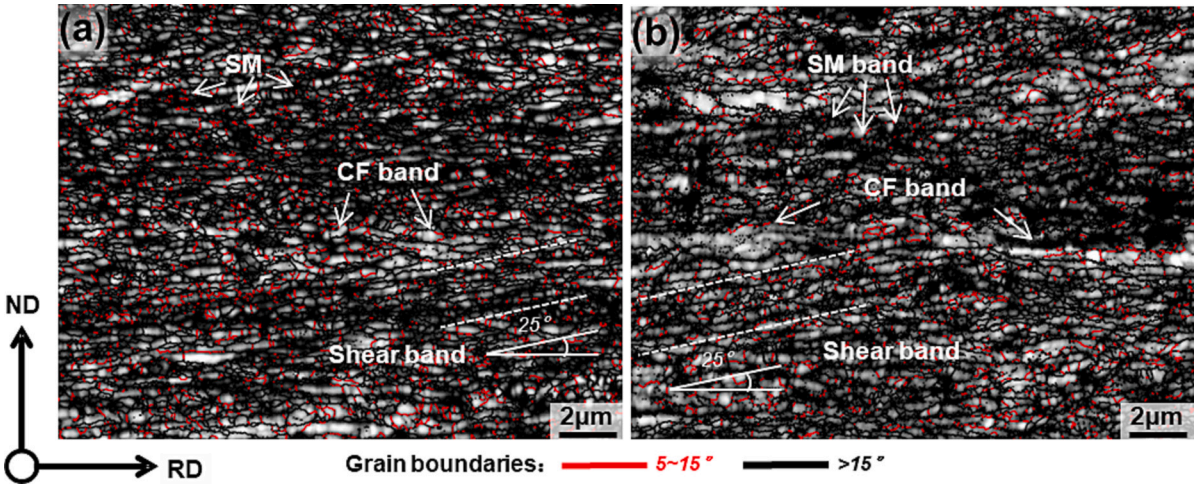

Fig. 2. EBSD results of the cold rolled samples. (a) and (b), the Image Quality (IQ) maps superimposed with the boundary of steels A and B, respectively. Here, the dark black region corresponds to SM, that is martensite generated from retained austenite due to strain-induced martensitic transformation (SIMT) during cold rolling deformation; Cold-worked ferrite (CF) is produced after severe plastic deformation of intercritical ferrite during cold rolling and is shown as the gray area in the IQ maps. The black lines represent high-angle grain boundaries (15°–62.8°), while the red lines are low-angle grain boundaries (5°–15°). (For interpretation of the references to colour in this figure legend, the reader is referred to the web version of this article.)

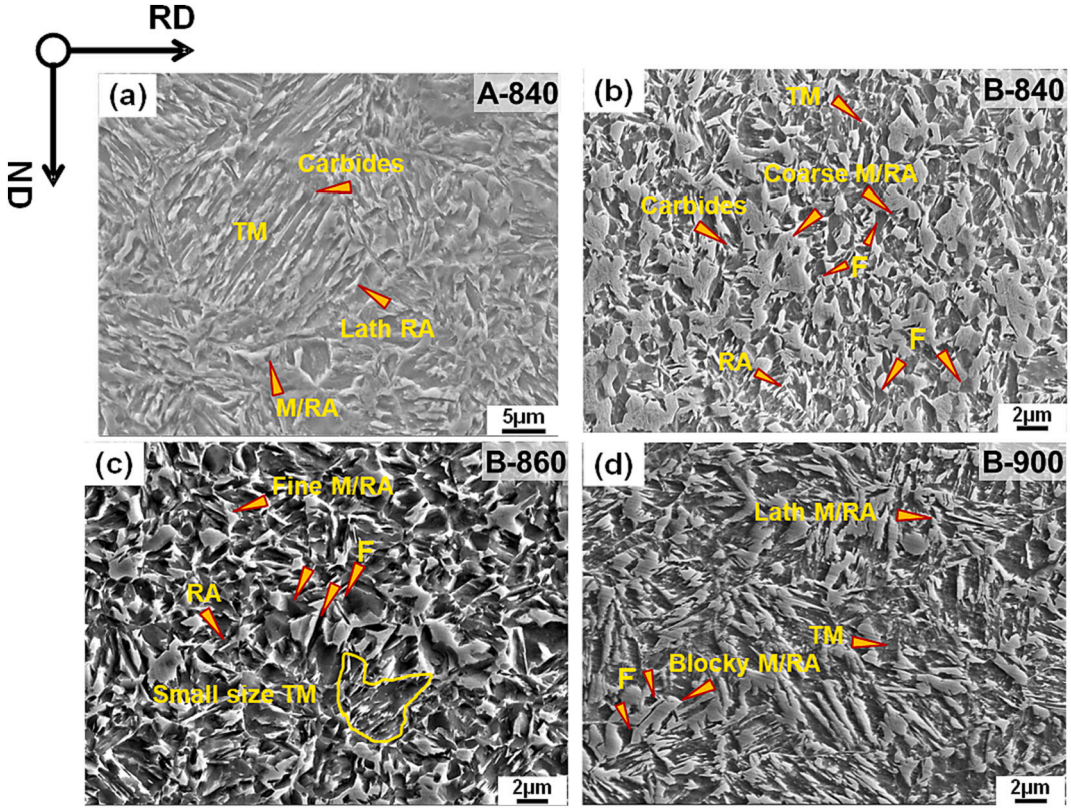

Fig. 3. SEM results of different samples (a) A-840, (b) B-840, (c) B-860, (d) B-900. F is ferrite; TM is tempered martensite produced during the initial quench; M/RA are the martensite-retained austenite islands.

significantly with the austenitization temperature. Compared with steel A, quenched and partitioned after complete austenitization, steel B always has ferrite over a wide intercritical austenitization range. After the Q&P process, the microstructure consists of ferrite, TM, and M/RA constituents. A large amount (~70%) of coarse M/RA constituents with a maximum width of ~4.7 μm is present in the microstructure of the B-840 sample (Fig. 3b). Equiaxed ferrite and a small amount of TM are distributed around the M/RA, and coarse M/RA borders the ferrite. With increasing austenitization temperature, the large blocky M/RA in the B-860 samples is gradually replaced by fine granular M/RA with equivalent grain diameter < 2 μm, (see Fig. 3c), as determined from the statistics of 15 SEM images. Except for low temperature austenitized samples, the M/RA morphology changes gradually from blocky or granular to lath-like morphology in B-880/900, but ferrite is still present. The fraction of TM in B-900 increases gradually (although it is similar to that of steel A), and the granular M/RA becomes increasingly elongated. The M/RA constituents exhibit discontinuous and fragmented morphologies, leading to a finer microstructure that steel A. The volume fraction of RA is determined via XRD and EBSD (see Table 2). In general, the RA content of steel B is higher than that of steel A. In addition, the fraction of RA in steel A seems to be more sensitive to changes in the austenitization temperature and decreases rapidly with increasing temperature.

Table 2
Volume fraction of RA based on EBSD and XRD data (%).

Measurement method	Austenitization temperature (°C)			
	840	860	880	900
Steel A, EBSD	14.6	11.2	11.0	9.2
XRD	11.5	9.2	7.7	8.4
Steel B, EBSD	14.1	14.5	14.1	12.7
XRD	23.5	19.3	15.7	14.3

3.3. Mechanical properties

Figure 4 presents an example of the tensile test results obtained after the steels have undergone the Q&P process. The corresponding mechanical properties are presented in Table 3. The UTS of each sample exceeds 1200 MPa, satisfying high strength requirements. The B-840 sample has the highest UTS (1522 MPa). In general, the UTS of each steel decreases gradually with increasing austenitization temperature, whereas the YS increases gradually. For steel A, the A-840 and the A-900 samples have the highest UTS (1379 MPa) and the lowest UTS (1277 MPa), respectively. The YS of steel B is significantly higher than that of

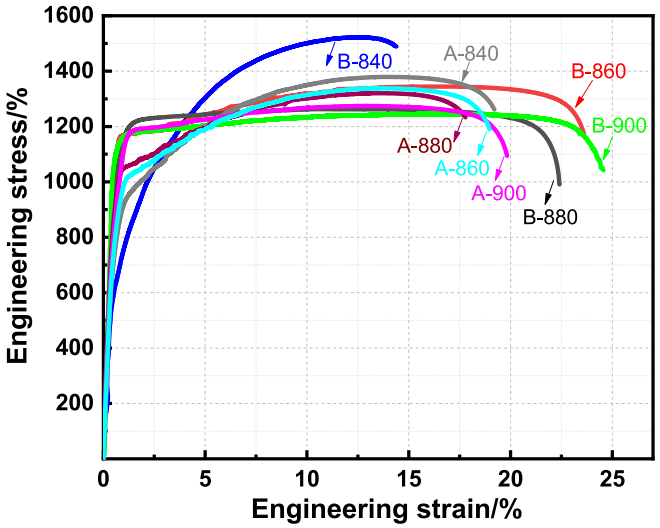

Fig. 4. Mechanical properties of the studied samples.

Table 3
Mechanical properties.

Samples	UTS (MPa)	YS (MPa)	TE (%)	PSE (GPa.%)
A-840	1379 ± 10	857 ± 12.4	19.2 ± 1.6	26.5 ± 2.0
A-860	1338 ± 8.2	921 ± 6.2	19 ± 1.4	25.4 ± 2.0
A-880	1320 ± 14.6	996 ± 34.7	17.8 ± 0.8	23.5 ± 1.4
A-900	1277 ± 1.6	1076 ± 51.5	20 ± 0.7	26.6 ± 0.9
B-840	1522 ± 26.9	710 ± 49.8	14.5 ± 0.6	22 ± 0.5
B-860	1345 ± 10.9	1163 ± 16.9	24 ± 0.85	32.3 ± 1.4
B-880	1263 ± 14.8	1169 ± 27.9	22.4 ± 2.3	28.3 ± 3.1
B-900	1246 ± 4.2	1124 ± 35.4	24.6 ± 1.6	30.6 ± 1.9

Mechanical properties in Table 3 are expressed as the average values of three tensile specimens for each processing (the standard deviations of the data are given). Here, 0.2% offset yield strength is used for YS statistics.

steel A, except for the B-840 sample, where the YS is 710 MPa. The results show that steel B exhibits better ductility (total elongation, TE > 20%) than steel A. In particular, the UTS and YS for the B-860 sample are 1345 MPa and 1163 MPa, respectively. The corresponding TE is high (24%), and accordingly the highest PSE (>32 GPa.%) is obtained for this sample. Similarly, an excellent strength-ductility match of 30.6 GPa.% is achieved for the B-900 sample, which has the highest TE (24.6%).

4. Discussion

4.1. Simulation of austenite transformation kinetics

To further understand the austenitization process of the two steels, numerical simulations of multi-phase conditions are performed using a DICTRA module. As shown in Fig. 5a, the assumption is that an austenite γ (A) core with a width of 1 nm, grows into the adjacent α, cold-worked ferrite (F), and martensite (M) simultaneously, based on a local equilibrium (LE) condition at the migration interface. The model obeys the law of mass conservation [44], and the correspondence between the diffusion velocity and diffusion flux at the γ/α phase interface is expressed as follows,

$$\frac{dx_i}{dt} = \frac{\left(J_i^{\gamma} - J_i^{\alpha}\right)}{\left(C_i^{\gamma^*} - C_i^{\alpha^*}\right)} \tag{1}$$

here, $C_i^{\gamma^*}$ and $C_i^{\alpha^*}$ are the concentrations of solid solution element i at the γ/α interface, wt%; x is the position of the interface, m; J_i^{γ} and J_i^{α} are the diffusion flux values of element i at the interface. The diffusion flux is defined by Fick's first law.

The most commonly observed lath width is 0.2 μm for 0.2 wt% C

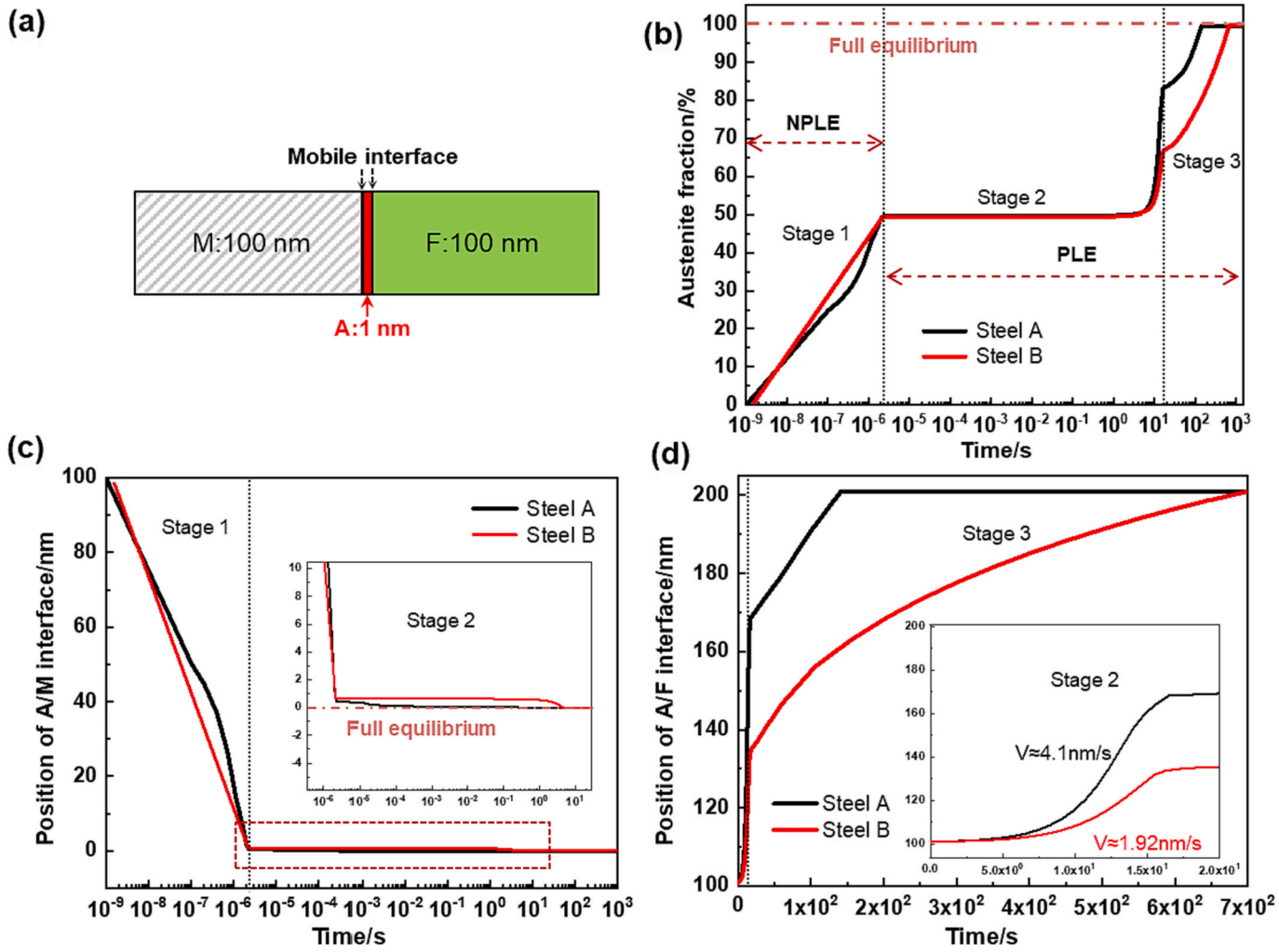

Fig. 5. (a) The model configuration of DICTRA, where austenite (A) undergoes reverse transformation from the middle to the cold-worked ferrite (F) and martensite (M) on both sides. Here, the half-lath width of ferrite and martensite are used, respectively. The initial composition of each phase is given in Table 4; (b) the absolute value of the volume fraction determined for austenite during the reverse transformation; (c) and (d) show the "position-time" relationship of the A/M (Austenite/Martensite) and A/F (Austenite/Ferrite) interfaces during heating and holding, respectively. This numerical simulation included heating from 660 °C to 825 °C at 10 °C/s for 1000 s.

martensite as reported [18]. Therefore, according to the phase ratio, ferrite is also defined as the same width. As shown in Fig. 5a, the size of M and F are set to half lath width of 100 nm, to simplify the calculation. The initial chemical composition of each unit is based on the thermodynamic calculation results (see Table 4). Note that cementite dissolution is assumed in this model, as the lack of corresponding thermodynamic data for Al-added medium-Mn steels results in non-convergence of the calculations. The heating temperature employed for the kinetic calculation (i.e., 825 °C) is sufficient for full austenitization, and the used heating rate (10 °C/s) is consistent with the actual heating rate.

Figure 5b shows the results of the kinetics associated with austenite transformation. In general, the plot of the austenite volume fraction vs. time for both steels can be divided into three successive stages, considering both the austenite-ferrite (A/F) and the austenite-martensite (A/M) interfaces simultaneously: ultra-fast stage 1 ($<2 \times 10^{-6}$ s), fast stage 2 (>2 s), and slow stage 3 (>20 s). This is consistent with the results of the inverse phase transformation kinetics of austenite in related literature [14,45]. The migration of each interface is plotted to clarify the growth of austenite to both sides of the interface (see Fig. 5c and d). Fig. 5c reflects the migration distance of austenite and adjacent martensite (A/M) as a function of time. As shown in the figure, in a very short time ($\sim 2 \times 10^{-6}$ s), the austenite quickly consumes almost the entire martensite (M) region, which corresponds to stage 1 in Fig. 5b. Luo et al. also obtained similar calculation results in 5Mn steel [14]. In this stage, similar trends are observed for steels A and B. In contrast, as indicated in Fig. 5d, almost no movement is observed at the A/F interface in both steels ($<2 \times 10^{-6}$ s). Following a period of 5 s delay, the migration of the A/F interface towards the ferrite side initiates gradually, under the partitioning local equilibrium (PLE) mode. These results provide strong evidence that the initial stage of austenitization is dominated by the migration of the A/M interface controlled by the negligible partitioning local equilibrium (NPLE) mode, and almost no movement occurs at the A/F interface. This concurs with the results shown in Fig. 3, where a large fraction of ferrite is observed. From this point of view, the presence of the A/F interface can effectively retard the coarsening of austenite grains and enhance the internal enrichment of elements, thus contributing to the thermodynamic stability of the parent austenite.

Moreover, it can be observed that the austenitization process of steel B lags behind that of steel A, consistent with the observations in section 3.2. Steel A exhibits a significantly faster austenitization process, completing it within approximately 150 s. However, steel B, Al-added, requires 700 s. The austenitization rate of the former is approximately 4.7 times faster than that of the latter (as shown in Fig. 5b). Similar findings were reported by Yu et al. [46]. in a simulation study involving only a single ferrite-austenite interface. They proposed that the addition of Al decelerates the interface movement during the initial NPLE stage, delaying the austenitization.

In contrast to their perspective, our results indicate that the addition of Al has minimal impact on the NPLE stage when considering the presence of the martensite interface (as shown in Fig. 5b). Conversely, as observed in stage 2, the interface migration rate of the Al-free steel A (4.1 nm/s) is approximately twice as fast as that of the Al-added steel B (1.92 nm/s). This phenomenon is more pronounced in stage 3. It can be inferred that adding Al significantly retards the kinetics of the A/F interface during the PLE stage. However, the underlying mechanism needs to be further studied in the future.

Table 4
Equilibrium chemical composition of γ and α phases (wt%).

Steels	Martensite&austenite				Ferrite			
	C	Mn	Si	Al	C	Mn	Si	Al
Reference steel A	0.41	7.99	1.51	/	0.004	2.3	1.6	/
Al-added steel B	0.48	8.99	1.27	0.61	0.004	2.34	1.02	1.28

4.2. Interaction between austenite formation and ferrite retention

In Fig. 3, a large amount of ferrite is observed in the Q&P samples (B-840/860) of steel B, whereas full austenitization has already been achieved in all samples of steel A. Therefore, to further study the austenitization and ferrite retention behavior of different steels, interrupted quenching (IQ) experiments were designed (see Fig. 1). The samples were quenched to room temperature immediately after heating to 650/750/840 °C.

Figure 6 shows that the interrupted quenching experiments can "freeze" the microstructure to room temperature for in-depth analysis. Steels A and B have undergone completely different recrystallization processes. Surprisingly, even in 0 s at a low temperature of 650 °C (Fig. 6a), a large amount of uniform equiaxed-shape ferrite is present in steel A. Meanwhile, as shown in Fig. 6c, the large blue area corresponds to the KAM value below 1°. These results indicate that the recrystallization of CF and SM is completed during the heating process. Furthermore, a considerable amount of micron-size austenite retained at room temperature is surrounded by many ferritic grains. Fig. 6b shows the microstructure of steel B annealed at the same thermal cycle. In contrast to the trends observed for steel A, numerous low-angle grain boundaries, usually indicating incomplete recrystallization [37], are observed in steel B. Like steel A, the austenite in B-IQ-1 sample is embedded in the middle of SM. This is due to the transformation of RA into SM during cold rolling and the strong crystallographic distortion, which increases the dislocation density in SM. In addition, SM inherits high concentrations of C and Mn from austenite. Thus, these dark SM regions will be the preferential sites for austenite nucleation, which is consistent with literature reports [45]. This can be confirmed in the KAM map as it fully reveals the degree of crystal deformation caused by high strain [47]. Here, the 2nd neighbor is used, and misorientations >5° are taken into account to remove the influence of adjacent boundaries. As shown in Fig. 6c, d, and h, the high KAM values are mainly distributed inside the RA grains and at the interface of RA and SM, which indicates that the RA is transformed from the previous SM, thus inheriting the high dislocation density. Moreover, B-IQ-1 sample has very low austenite content with significantly refined grains (<0.5 μm). These results confirm the DICTRA calculation results, where the austenite growth rate of steel B lags behind that of A.

Increasing the non-isothermal temperature increases the proportion of martensite in steel A. No austenite survives to room temperature in the A-IQ-2/3 samples. Especially after non-isothermal quenching at 840 °C (A-IQ-3), the microstructure consists of fully martensite (Fig. 7a). This implies that steel A has undergone rapid and complete recrystallization and austenitization during the heating stage. It can be attributed to two factors: *(i)* a high degree of austenitization, which dilutes the average content of C and Mn in itself and *(ii)* a progressive coarsening of the austenite grain size. These two factors reduce the thermal stability of austenite, which transforms easily and more completely (compared with transformation at higher stabilities) to martensite during cooling.

In Fig. 6e and f, the A-IQ-2 sample contains a large amount of martensitic at room temperature, indicating it is highly austenitized. In contrast, the B-IQ-2 sample consists of a great deal of banded CF, containing low-angle grain boundaries, with a maximum length and width of 19.4 μm and 8 μm, respectively, in the current field of view. Due to the poor quality of Kikuchi, the colour of this part of the CF is dark, indicating that steel B did not undergo sufficient recrystallization. This result is consistent with the recrystallization retardation of similar composition medium-Mn steel (5Mn-1.1Al, wt%), reported by Suh et al. [37]. Plenty of austenite was successfully retained at room temperature in the B-IQ-2/3 samples. The stability of austenite has been reported to depend on chemical composition and grain size [30]. Considering that the C

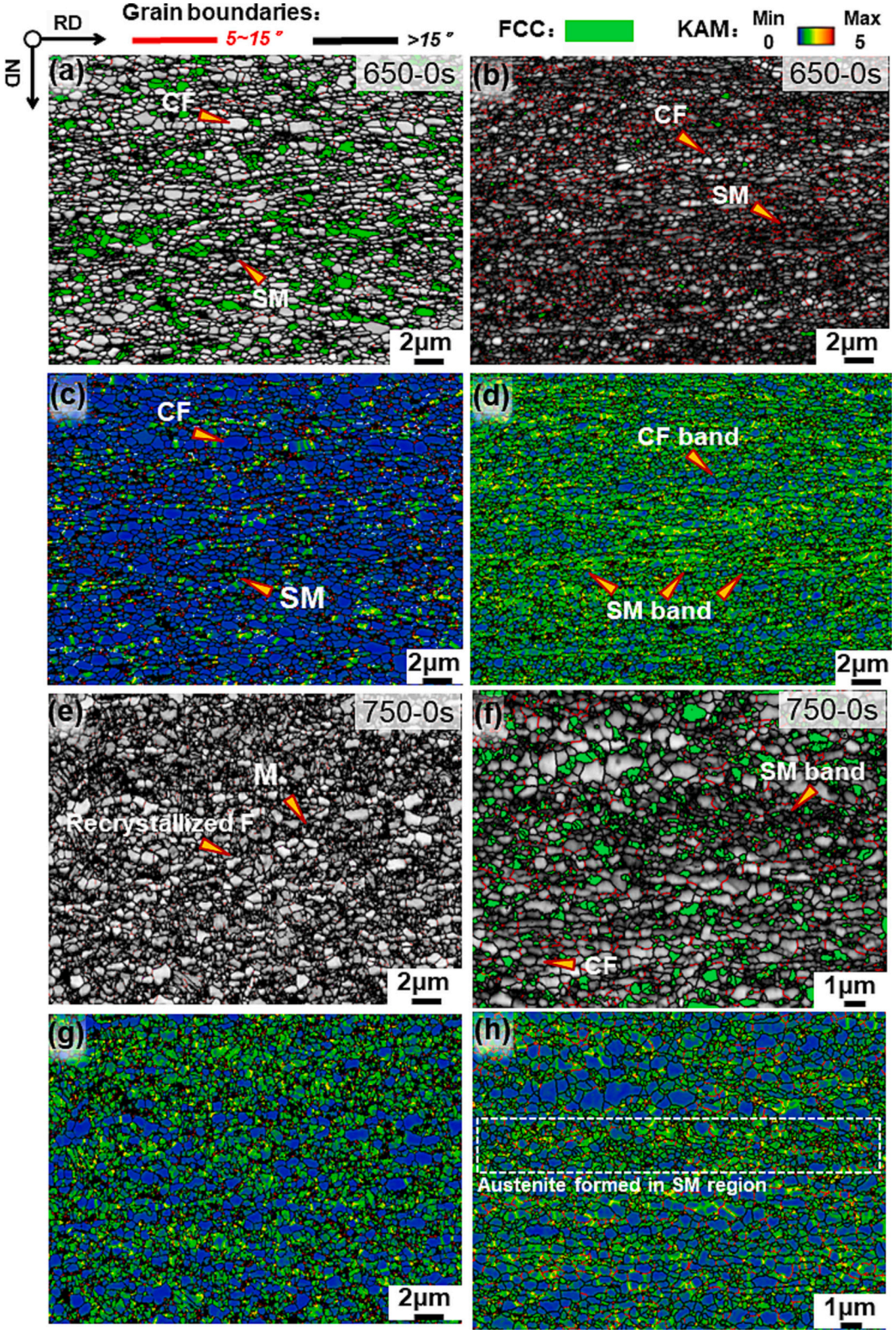

Fig. 6. EBSD characterization of interrupted quenching (IQ) microstructure. (a) A-IQ-1, (b) B-IQ-1, (c) and (d) show the corresponding Kernel average misorientation (KAM) results, respectively. (e) A-IQ-2, (f) B-IQ-2, (g) and (h) show the corresponding KAM maps, respectively. The 2nd neighbor approach is employed, and misorientations exceeding 5° are considered to mitigate the influence of neighboring boundaries on the calculation results. The black lines are high-angle boundaries (misorientation angle: 15°–62.8°), while the red lines are low-angle boundaries (misorientation angle: 5°–15°). SM: the martensite generated from retained austenite due to strain-induced martensitic transformation (SIMT) during cold rolling deformation. Cold-worked ferrite (CF) is produced after severe plastic deformation of intercritical ferrite during cold rolling. (For interpretation of the references to colour in this figure legend, the reader is referred to the web version of this article.)

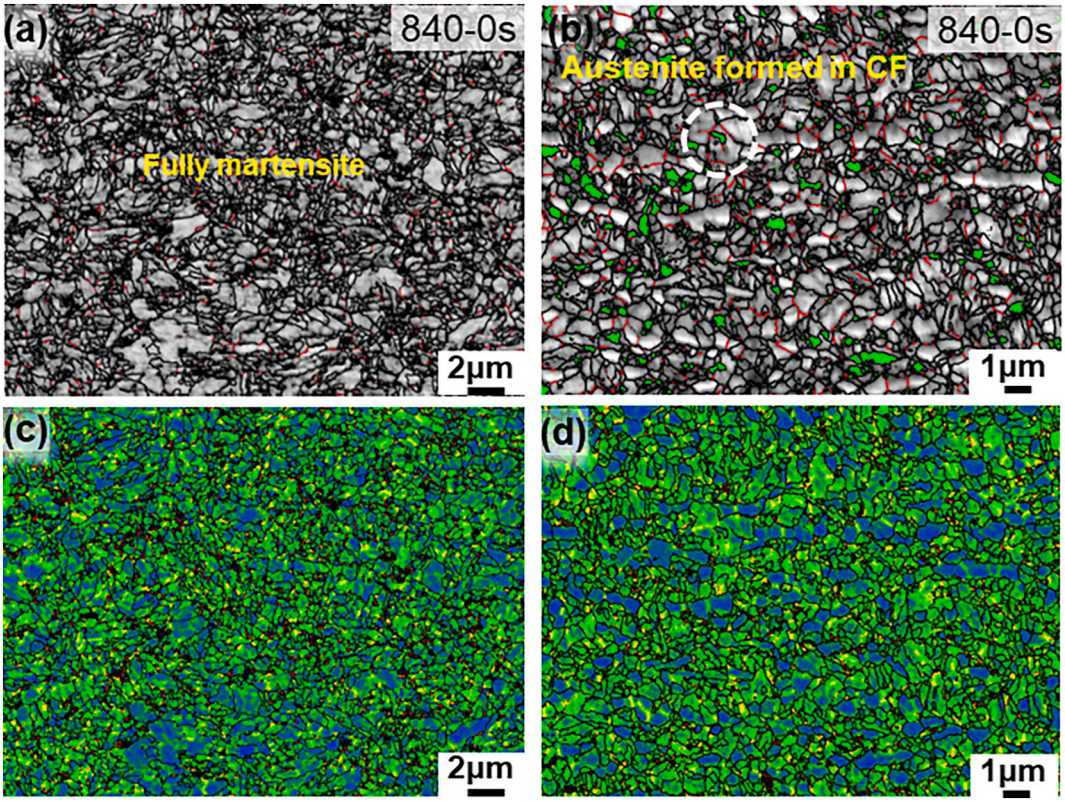

Fig. 7. Results of EBSD characterization of interrupted quenching microstructure. (a) A-IQ-3, (b) B-IQ-3, (c) and (d) show the KAM results of (a) and (b), respectively.

diffusion rate in the heating stage is approximately the same, grain size refinement contributes the most to the stability of austenite. Furthermore, almost no austenite transformation occurs inside the CF, and only very fine austenite nucleates between the SM and CF interface and grows slowly into the ferrite. As shown by the white circle in Fig. 7b, the austenitic transformation does not start inside the CF in steel B until the peak temperature reaches 840 °C. This is very consistent with the numerical simulation results in Section 4.1, that is, the ferrite interface retards the growth of austenite. Based on these results, it is reasonable to conclude that CF plays a very important role in the austenite transformation. On the one hand, recovery and recrystallization of CF compete with austenitization, resulting in delayed austenitization. On the other hand, a large amount of CF will further suppress austenite grain coarsening, thereby refining the structure.

4.3. Influence of cold-worked ferrite on the microstructure

4.3.1. Microstructure observation and analysis via TEM

To further reveal the microstructure, typical samples are characterized via TEM. As shown in Fig. 8a-b, RA with various morphologies (granular, lath, and film) are distinguishable in the B-860 sample. Previous work has confirmed that multi-morphological RA can adapt to small strains and continue to experience the TRIP effect [48], which overcomes the insufficient plasticity of traditional Q&P steels. In particular, the RA films between martensitic laths have a higher carbon content than other RA regions [49]. These films are shielded by the stress and hydrostatic pressure of the surrounding martensitic laths, and are therefore more stable than the blocky type of RA. M/RA islands are also observed in the B-840 sample, but these islands are significantly larger than those in the B-860 sample. The B-840 sample contains blocky M/RA with a diameter of ~4.3 μm, where the RA is mainly embedded in the M (Fig. 8e, f), consistent with the SEM observations. The microstructure of A-840 is mainly composed of lath TM, with numerous dislocations. As seen in Fig. 8g-i, RA with lath-like morphology is mainly located at the martensite laths, consistent with the SEM and EBSD observations.

4.3.2. Crystallographic analysis of martensite

From the TEM results, ferrite's presence significantly impacts RA's characteristics, resulting in multi-morphologies. Therefore, the crystallographic characteristics of the A/B-840 sample are further analyzed. Fig. 9a shows that when the RA of B-840 is adjacent to ferrite, it assumes a granular or blocky morphology characterized by γ1 and γ2. Simultaneously, γ1 and γ2 exhibit arc-shaped growth towards the F1, where the phase boundaries manifest as high-angle grain boundaries (32.3° and 50.97°, respectively). As mentioned above, this type of austenite is probably produced during annealing, attributed to its gradual growth towards the ferrite. Conversely, when RA is positioned within the martensite lath, it adopts a lath-like morphology as γ3 and γ4. Moreover, RA adjacent to the ferrite usually appears as a twinned morphology, such as γ1 and γ5-γ8. Prior studies [50] have reported the frequent occurrence of twinned austenite in high Mn and C steels. This supports evidence that cold-worked ferrite facilitates elements partitioning during the heating and annealing. In contrast, the RA observed in A-840 predominantly follows the K—S relationship with the surrounding TM, exhibiting a consistent lath morphology, as depicted in Fig. 9b.

Moreover, the average size of the parent austenite grain (PAG) in A-840 sample is ~15 μm, approximately three times larger than that of B-840. Fig. 9c and d reveal that the variants in B-840 exhibit a more random distribution with a small size (width < 1.5 μm). In contrast, there is a strong variant selection in A-840, and the block is significantly coarsened. Notably, the V12&V4 variant pair reaches 14.3 μm and 4.5 μm in length and width, respectively. Previous investigations have demonstrated that high C content can substantially reduce the size of martensitic blocks [51]. Therefore, this result can reasonably be explained by the high carbon content in B-840 PAG due to the retention of the ferrite. Furthermore, the limited PAG size of the B-840 sample further restricts the formation of large single variants according to

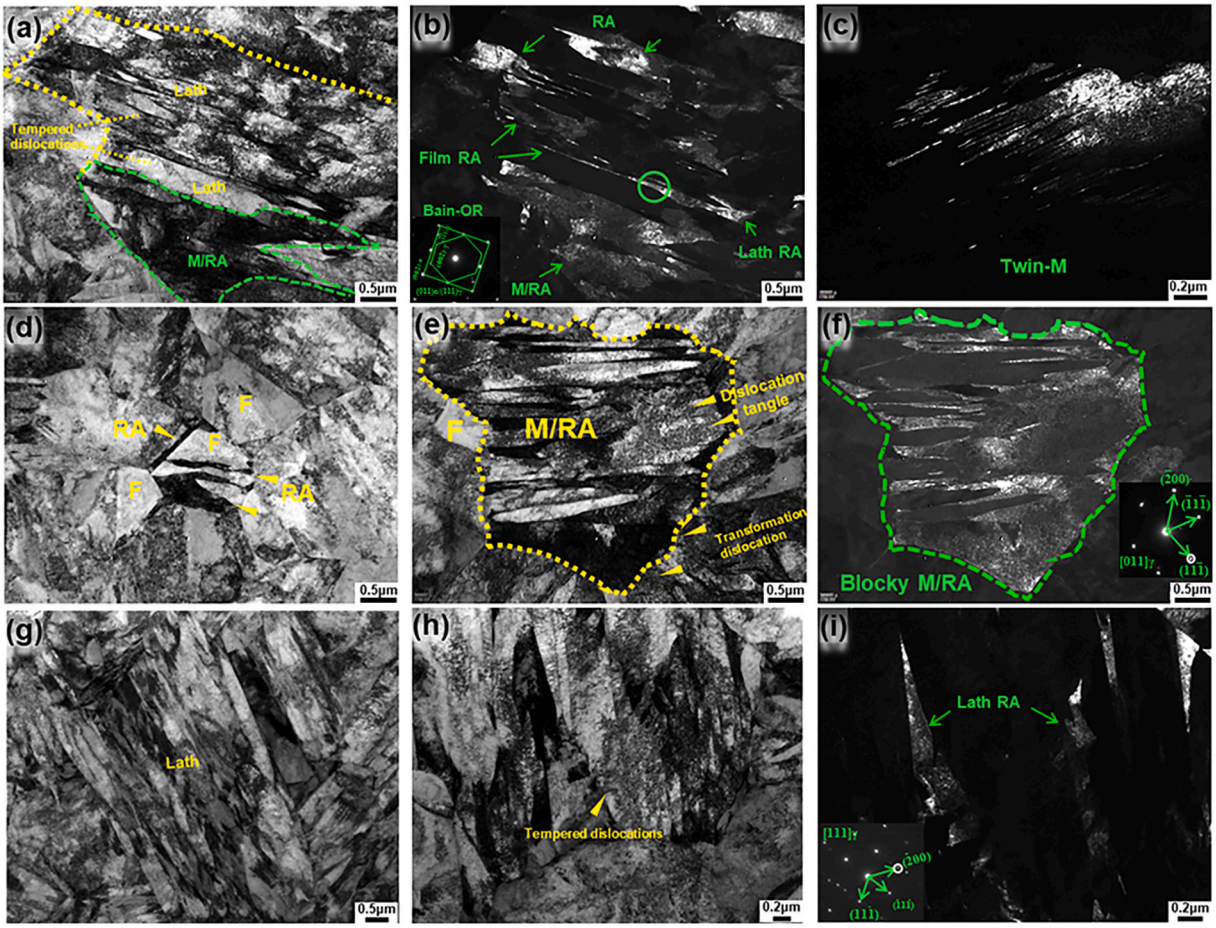

Fig. 8. TEM micrographs showing different martensite and RA morphology: (a)–(c) B-860 sample, (a) bright field TEM result, (b) dark field TEM result of (a) and corresponding selected area electron diffraction pattern, (c) dark field image of fresh martensite. (d)–(f) B-840 sample, (d) bright field image of the microstructure, (e) bright field image of M/RA, (f) dark field image of (e) and corresponding selected area electron diffraction (SAED) pattern. (g)–(i) A-840 sample, (g) and (h) bright field image of TM, and (i) dark field image of lath RA and corresponding SAED pattern.

elastic strain energy theory [52]:

$$\Delta E_V = 1276.1\left(\frac{x}{d}\right)^2 + 562.6\left(\frac{x}{d}\right) \tag{2}$$

here, ΔE_V is the increase in elastic strain energy; x and d are the thickness of martensite lath and parent austenite grain size, respectively.

Thus, in contrast to steel A with significant variants selection, the presence of cold-worked ferrite has a profound impact on the martensite substructure. It enhances the carbon partitioning effect and effectively constrains the size of the PAG, resulting in the formation of randomly distributed and fine martensitic blocks. This mechanism explains the finer TM and M/RA observed in steel B.

4.4. Analysis of mechanical performance

In Fig. 4, the UTS of steels A and B decreases gradually with increasing austenitization temperature, whereas the YS gradually increases, and the max TE of both steels is achieved after austenitization at 900 °C. This can be attributed to the fact that elevated annealing temperature reduces the thermal stability of prior austenite, leading to an increase in the amount of TM obtained after quenching at a given quenching temperature ($T = 150$ °C). This TM provides a good combination of significant elongation and high YS. An abnormal UTS and the worst ductility are obtained for sample B-840 with the least amount of TM and many blocky M/RA islands. The above analysis has been elaborated in our previous work [53]. It should be pointed out that, except for the B-840 sample, steel B exhibits a significant increase in YS. For instance, after the same thermal cycle, B-860 shows a remarkable YS increase of 242 MPa compared to A-860. This improvement can be attributed to the finer blocks in steel B (Fig. 9), which contribute to a higher number of effective grain boundaries when compared to steel A with coarser blocks.

Figure 10 shows the instantaneous work hardening rate curves of the two steels after different Q&P processes. The sudden increase in the hardening rate of different samples (shown by the red arrows) is attributed to the TRIP effect [54]. Owing to the differences among the stabilities of RA, the duration and severity of this effect differ significantly among the samples. The TRIP effect of steel A occurs mainly at logarithmic strain $\varepsilon < 10$, with almost no hardening phenomenon in the subsequent stage. In contrast, steel B still exhibits TRIP effect in the later stage ($\varepsilon > 10$), which is attributed to various RA (Fig. 8), and is characterized by significant enrichment of Mn and C elements.

In summary, as shown in Fig. 11, the cold-worked ferrite is deliberately introduced via IA and cold rolling prior to the heat treatment process. Compared with the steel containing only Si, the Al-added medium-Mn steel retains this ferrite over a wide temperature range. This ferrite will trigger complex coupling effects, which will have a crucial impact on the final microstructure and mechanical properties: *(i)* recrystallisation and austenitization of cold-worked ferrite compete with each other during heating, resulting in delayed austenitization; *(ii)* the ferrite retained to high temperature prevents excessive coarsening of austenite, thereby producing a finer microstructure; and *(iii)* cold-worked ferrite leads to the formation of various austenite morphologies as well as refinement in the size of martensite units. All the above

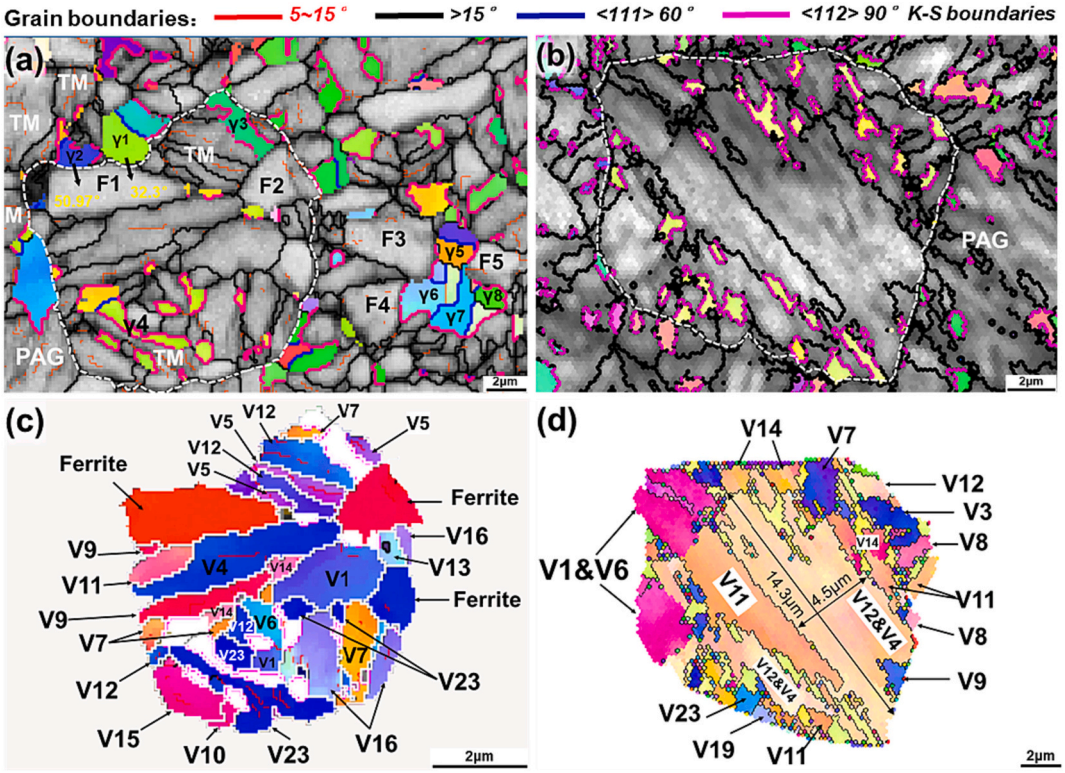

Fig. 9. (a) and (b) combined IQ and ND-inverse pole figure (IPF) map of RA in B/A-840 samples, respectively. (c) and (d) crystallographic analysis of martensite of B/A-840 sample, respectively. Special grain boundaries, such as twin boundaries and Kurdjumov-Sachs (K—S) relationships, are indicated by blue and purple lines, respectively.

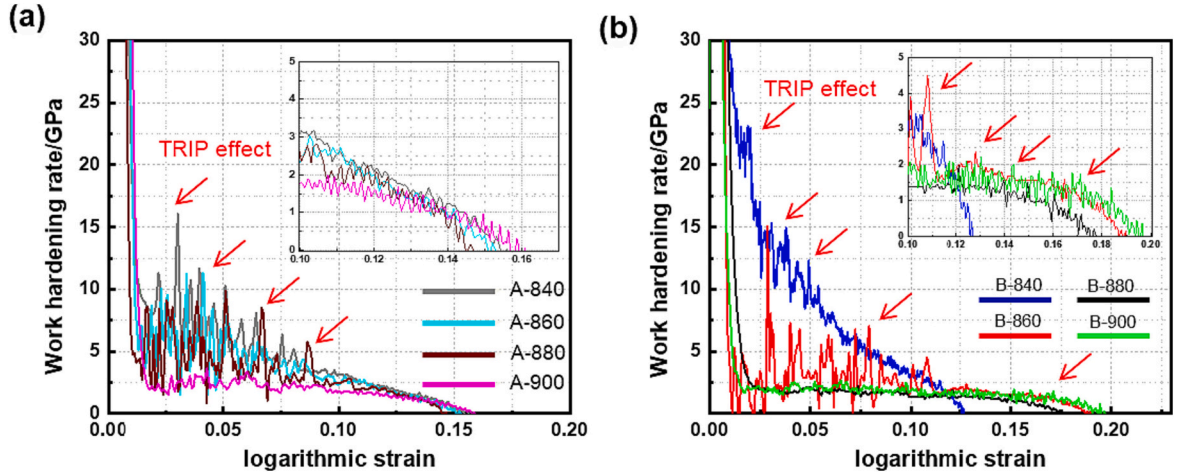

Fig. 10. Instantaneous work hardening rate of different steels, (a) and (b) correspond to steel A and steel B samples, respectively.

factors lead to the desired strength-ductility balance.

5. Summary and conclusions

In this work, the effect of cold-worked ferrite, existing prior to the heat treatment process on the microstructure and mechanical properties is investigated. The main contributions of this work can be summarized as:

1. The cold-worked ferrite significantly refines and fragments the parent austenite, thereby reducing the martensite block size. Consequently, a microstructure composed of numerous uniformly dispersed M/RA (diameter < 2 μm) and small tempered martensitic grains (diameter ~ 3 μm) with a fine and complex morphology can be formed.
2. Controlled by the PLE mode, austenitization in the cold-worked ferrite is significantly delayed during heating, thereby refining the parent austenite grains. Meanwhile, the competition between austenite nucleation and recrystallization during the reverse transformation further limits austenitization dynamics.
3. The cold-worked ferrite effectively restricts the size of the parent austenite and facilitates carbon partitioning, thereby preventing variant selection and coarsening. The small-sized variants with a randomized distribution greatly increase the number of block boundaries, resulting in a maximum improvement in YS of 242 MPa.

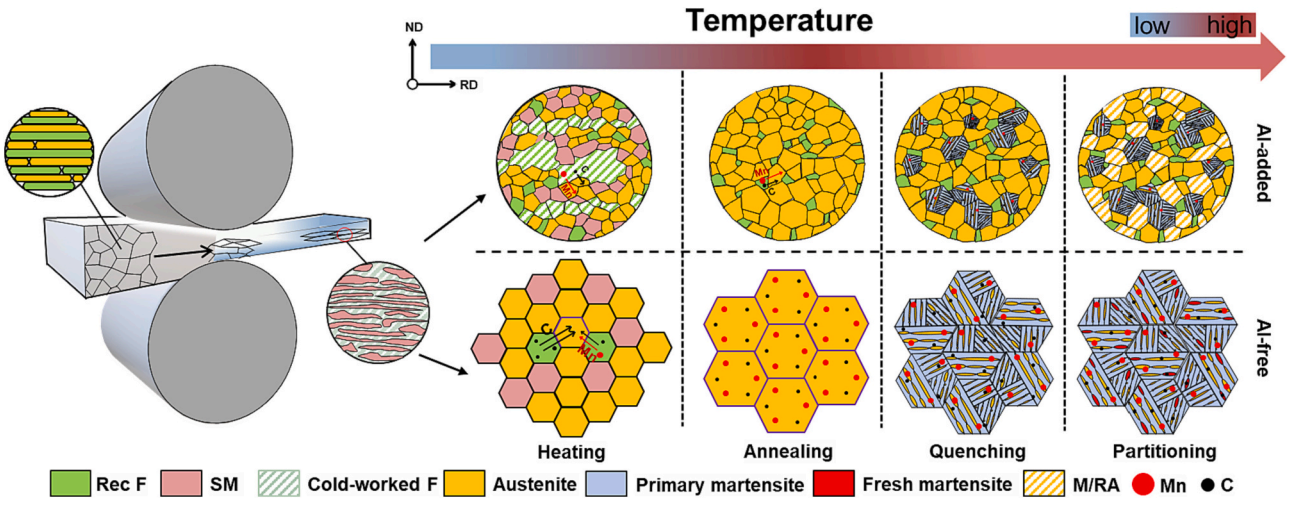

Fig. 11. Schematic showing the critical role of cold-worked ferrite on the microstructural evolution. Here, recrystallized cold-worked ferrite and the martensite produced by strain-induced martensite transformation (SIMT) of retained austenite are abbreviated as Rec F and SM, respectively.

4. The cold-worked ferrite results in diversified types of RA, significantly enhancing the strength-ductility balance of the Al-added steel, reaching the levels of the UTS increase from 1246 MPa to 1522 MPa. The best PSE measured for Al-added steel is ~32.3 GPa%, which is considerably higher than that of steel A without the cold-worked ferrite component (26.6 GPa %).

Declaration of Competing Interest

There are no known competing financial interests or personal relationships that could have appeared to influence the work reported in this paper.

Data availability

The raw/processed data required to reproduce these findings cannot be shared at this time as the data also forms part of an ongoing study.

Acknowledgments

This research was supported by the National Natural Science Foundation of China (Nos. 51974085 and 51674080), National Key Research and Development Program of China (2017YFB0304105, 2017YFB0304400) and Key R&D Program of Shandong Province (2019TSLH0103). At the same time, Jiayu expressed his gratitude for the funding granted by the China Scholarship Council (Student ID: 202106080027).

References

[1] N. Fonstein, Advanced High Strength Sheet Steels, Springer International Publishing, 2015.
[2] D.K. Matlock, J.G. Speer, Third generation of AHSS: Microstructure design concepts, in: Microstructure and Texture in Steels, Springer, London, 2009, pp. 185–205, https://doi.org/10.1007/978-1-84882-454-6_11.
[3] H. Aydin, E. Essadiqi, I.H. Jung, S. Yue, Development of 3rd generation AHSS with medium Mn content alloying compositions, Mater. Sci. Eng. A 564 (2013) 501–508, https://doi.org/10.1016/j.msea.2012.11.113.
[4] Y.K. Lee, J. Han, Current opinion in medium manganese steel, Mater. Sci. Technol. 31 (7) (2015) 843–856, https://doi.org/10.1179/1743284714Y.0000000722.
[5] D.W. Suh, S.J. Kim, Medium Mn transformation-induced plasticity steels: recent progress and challenges, Scr. Mater. 126 (2017) 63–67, https://doi.org/10.1016/j.scriptamat.2016.07.013.
[6] B.H. Sun, F. Fazeli, C. Scott, N. Brodusch, R. Gauvin, S. Yue, The influence of silicon additions on the deformation behavior of austenite-ferrite duplex medium manganese steels, Acta Mater. 148 (2018) 249–262, https://doi.org/10.1016/j.actamat.2018.02.005.
[7] J. Shi, X.J. Sun, M.Q. Wang, W.J. Hui, H. Dong, W.Q. Cao, Enhanced work-hardening behavior and mechanical properties in ultrafine-grained steels with large-fractioned metastable austenite, Scr. Mater. 63 (8) (2010) 815–818, https://doi.org/10.1016/j.scriptamat.2010.06.023.
[8] J. Hu, X.Y. Li, Q.W. Meng, L.Y. Wang, Y.Z. Li, W. Wei, Tailoring retained austenite and mechanical property improvement in Al–Si–V containing medium Mn steel via direct intercritical rolling, Mater. Sci. Eng. A 855 (2022), 143904, https://doi.org/10.1016/j.msea.2022.143904.
[9] Y. Zou, Y. Han, H.S. Liu, H.X. Teng, M.S. Qiu, F. Yang, Microstructure evolution and enhanced mechanical properties of a novel Nb-Ti micro-alloyed medium-Mn steel, Mater Charact 187 (2022), 111828, https://doi.org/10.1016/j.matchar.2022.111828.
[10] R. Zhang, W.Q. Cao, Z.J. Peng, J. Shi, H. Dong, C.X. Huang, Intercritical rolling induced ultrafine microstructure and excellent mechanical properties of the medium-Mn steel, Mater. Sci. Eng. A 583 (2013) 84–88, https://doi.org/10.1016/j.msea.2013.06.067.
[11] D.T. Han, Y.B. Xu, R.D. Liu, F. Peng, Y. Zou, W.H. Sun, Improving Mn partitioning and mechanical properties through carbides-enhancing pre-annealing in Mn-reduced transformation-induced plasticity steel, Scr. Mater. 187 (2020) 274–279, https://doi.org/10.1016/j.scriptamat.2020.06.027.
[12] Z.P. Hu, Y.B. Xu, Y. Zou, R.D.K. Misra, D.T. Han, S.Q. Chen, D.Y. Hou, Effect of intercritical rolling temperature on microstructure-mechanical property relationship in a medium Mn-TRIP steel containing δ ferrite, Mater. Sci. Eng. A 720 (2018) 1–10, https://doi.org/10.1016/j.msea.2018.02.052.
[13] Q.H. Han, Y.L. Zhang, L. Wang, Effect of annealing time on microstructural evolution and deformation characteristics in 10Mn1.5Al TRIP steel, Metallurgical and Materials Transactions A 46 (2015) 1917–1926, https://doi.org/10.1007/s11661-015-2822-7.
[14] H.W. Luo, J. Shi, C. Wang, W.Q. Cao, X.J. Sun, H. Dong, Experimental and numerical analysis on formation of stable austenite during the intercritical annealing of 5Mn steel, Acta Mater. 59 (10) (2011) 4002–4014, https://doi.org/10.1016/j.actamat.2011.03.025.
[15] B.H. Sun, Y. Ma, N. Vanderesse, R.S. Varanasi, W.W. Song, P. Bocher, D. Ponge, D. Raabe, Macroscopic to nanoscopic in situ investigation on yielding mechanisms in ultrafine grained medium Mn steels: role of the austenite-ferrite interface, Acta Mater. 178 (2019) 10–25, https://doi.org/10.1016/j.actamat.2019.07.043.
[16] J.G. Speer, D.K. Matlock, B.C. De, J.G. Schroth Cooman, Carbon partitioning into austenite after martensite transformation, Acta Mater. 51 (9) (2003) 2611–2622, https://doi.org/10.1016/S1359-6454(03)00059-4.
[17] A.J. Clarke, J.G. Speer, M.K. Miller, R.E. Hackenberg, D.V. Edmonds, D.K. Matlock, F.C. Rizzo, K.D. Clarke, E. De, Moor., Carbon partitioning to austenite from martensite or bainite during the quench and partition (Q&P) process: a critical assessment, Acta Mater. 56 (1) (2008) 16–22, https://doi.org/10.1016/j.actamat.2007.08.051.
[18] A.J. Clarke, J.G. Speer, D.K. Matlock, F.C. Rizzo, D.V. Edmonds, M.J. Santofimia, Influence of carbon partitioning kinetics on final austenite fraction during quenching and partitioning, Scr. Mater. 61 (2) (2009) 149–152, https://doi.org/10.1016/j.scriptamat.2009.03.021.
[19] G.A. Thomas, J.G. Speer, D.K. Matlock, Quenched and partitioned microstructures produced via Gleeble simulations of hot-strip mill cooling practices, Metall. Mater. Trans. A 42 (12) (2011) 3652–3659, https://doi.org/10.1007/s11661-011-0648-5.
[20] Y. Toji, G. Miyamoto, D. Raabe, Carbon partitioning during quenching and partitioning heat treatment accompanied by carbide precipitation, Acta Mater. 86 (2015) 137–147, https://doi.org/10.1016/j.actamat.2014.11.049.
[21] R. Ding, D. Tang, A.M. Zhao, H. Guo, J.G. He, C. Zhi, Effect of ultragrain refinement on quenching and partitioning steels manufactured by a novel method, Mater. Des. 87 (2015) 640–649, https://doi.org/10.1016/j.matdes.2015.08.073.
[22] F. Peng, Y.B. Xu, D.T. Han, X.L. Gu, J.Y. Li, X. Wang, Influence of pre-tempering treatment on microstructure and mechanical properties in quenching and

partitioning steels with ferrite-martensite start structure, Mater. Sci. Eng. A 756 (2019) 248–257, https://doi.org/10.1016/j.msea.2019.04.047.
[23] E. De, J.G. Moor, D.K. Speer, J.H. Matlock, S.B. Lee Kwak, Effect of carbon and manganese on the quenching and partitioning response of CMnSi steels, ISIJ Int. 51 (1) (2011) 137–144, https://doi.org/10.2355/isijinternational.51.137.
[24] X.X. Dong, Y.F. Shen, N. Jia, Y.T. Zhu, Improving mechanical properties and retained-austenite stability of a medium carbon Q&P steel by adjusting phase ratio, Mater. Sci. Eng. A 833 (2022), 142580, https://doi.org/10.1016/j.msea.2021.142580.
[25] X.Q. Rong, S.L. Liu, Y.S. Li, B. Hu, M. Enomoto, H. Guo, C.J. Shang, Simultaneous enhancement of strength and ductility via rjr and ultrafine filmy retained austenite in a novel quench-partitioned and tempered steel, Mater. Sci. Eng. A 760 (2019) 47–57, https://doi.org/10.1016/j.msea.2019.05.064.
[26] W. Fu, C.N. Li, R. Duan, H.S. Gao, X.J. Di, D.P. Wang, Formation mechanism of CuNiAl-rich multi-structured precipitation and its effect on mechanical properties for ultra-high strength low carbon steel obtained via direct quenching and tempering process, Mater. Sci. Eng. A 833 (2022), 142567, https://doi.org/10.1016/j.msea.2021.142567.
[27] N. Zhong, X.D. Wang, L. Wang, Y.H. Rong, Enhancement of the mechanical properties of a Nb-microalloyed advanced high-strength steel treated by quenching–partitioning–tempering process, Mater. Sci. Eng. A 506 (1–2) (2009) 111–116, https://doi.org/10.1016/j.msea.2008.11.014.
[28] G.H. Gao, H. Zhang, X.L. Gui, P. Luo, Z.L. Tan, B.Z. Bai, Enhanced ductility and toughness in an ultrahigh-strength Mn–Si–Cr–C steel: the great potential of ultrafine filmy retained austenite, Acta Mater. 76 (2014) 425–433, https://doi.org/10.1016/j.actamat.2014.05.055.
[29] B.C. De, S.J. Cooman, S.M. Lee, E.J. Shin, J.G. Speer Seo, Combined intercritical annealing and Q&P processing of medium Mn steel, Metallurgical and Materials Transactions A 48 (1) (2017) 39–45, https://doi.org/10.1007/s11661-016-3821-z.
[30] L. Cho, E.J. Seo, B.C. De, Cooman., Near-Ac3 austenitized ultra-fine-grained quenching and partitioning (Q&P) steel, Scr. Mater. 123 (2016) 69–72, https://doi.org/10.1016/j.scriptamat.2016.06.003.
[31] J. Mahieu, S. Claessens, B.C. De Cooman, Galvanizability of high-strength steels for automotive applications, Metallurgical and Materials Transactions 32 (11) (2001) 2905–2908, https://doi.org/10.1007/s11661-001-1042-5.
[32] I. Hertveldt, B.C. De Cooman, S. Claessens, Influence of annealing conditions on the galvanizability and galvannealing properties of TiNb interstitial-free steels, strengthened with phosphorous and manganese, Metall. Mater. Trans. A 31 (4) (2000) 1225–1232, https://doi.org/10.1007/s11661-000-0118-y.
[33] D.H. Kim, J.H. Kang, J.H. Ryu, S.J. Kim, Enhancement of tensile properties by room-temperature quenching and partitioning of 0.2C–10Mn–2Al steel, Mater. Sci. Technol. 35 (17) (2019) 2115–2119, https://doi.org/10.1080/02670836.2018.1522101.
[34] Z.L. Wu, C.N. Jing, Y. Feng, Z.T. Li, T. Lin, J.R. Zhao, L. Liu, Effect of a new pretreatment-Q&P process on the microstructure and mechanical properties of light-weight Al-containing medium-Mn steels, Mater. Sci. Eng. A 862 (2023), 144468, https://doi.org/10.1016/j.msea.2022.144468.
[35] S. Kaar, D. Krizan, R. Schneider, C. Sommitsch, Impact of Si and Al on microstructural evolution and mechanical properties of lean medium manganese quenching and partitioning steels, Steel Res. Int. 91 (10) (2020) 2000181, https://doi.org/10.1002/srin.202000181.
[36] S. Yan, T.L. Li, Z.G. Xu, T.S. Liang, S. Wang, X.H. Liu, Experimental evidence for "double-edged sword" effect of the fibrous δ-ferrite on mechanical properties: a case study of Fe-5.95Mn-1.55Si-1.0Al-0.055C medium-Mn steel, J. Mater. Res. Technol. 18 (2022) 3834–3840, https://doi.org/10.1016/j.jmrt.2022.04.077.
[37] D.W. Suh, S.J. Park, T.H. Lee, C.S. Oh, S.J. Kim, Influence of Al on the microstructural evolution and mechanical behavior of low-carbon, manganese transformation-induced-plasticity steel, Metallurgical and Materials Transactions A 41 (2) (2010) 397–408, https://doi.org/10.1007/s11661-009-0124-7.
[38] A. Chbihi, D. Barbier, L. Germain, A. Hazotte, M. Goune, Interactions between ferrite recrystallization and austenite formation in high-strength steels, J. Mater. Sci. 49 (10) (2014) 3608–3621, https://doi.org/10.1007/s10853-014-8029-2.
[39] R. Ueji, N. Tsuji, Y. Minamino, Y. Koizumi, Ultragrain refinement of plain low carbon steel by cold-rolling and annealing of martensite, Acta Mater. 50 (16) (2002) 4177–4189, https://doi.org/10.1016/S1359-6454(02)00260-4.
[40] H.B. Pan, W.M. Liu, H.T. Wang, Y.G. Liu, Y.Q. Tian, K. Chen, X.H. Shen, H. Zhang, X.Y. Mao, Y.Y. Xiao, D.Y. Li, Understanding crystallographic orientation, microstructure and mechanical properties dependent interaction between recrystallization and phase transformation of a Fe–Al–Mn–Mo–C dual-phase steel, J. Mater. Res. Technol. 15 (2021) 6190–6203, https://doi.org/10.1016/j.jmrt.2021.11.064.
[41] S.C. Liu, H.K. Dong, Y.B. Li, Z.G. Yang, H. Chen, Flash annealing enables 1 GPa nanoprecipitate-strengthened "NANOHITEN" ferritic steels, Mater. Sci. Eng. A 861 (2022), 144364, https://doi.org/10.1016/j.msea.2022.144364.
[42] S.Q. Chen, Control of Microstructure Evolution and Mechanical Properties of ART-Annealed Medium Manganese Steel, Northeastern University, Liaoning, 2017.
[43] A.L. Titchener, M.B. Bever, The stored energy of cold work, Prog. Met. Phys. 7 (1958) 247–338, https://doi.org/10.1016/0502-8205(58)90006-6.
[44] T.C. Illingworth, I.O. Golosnoy, V. Gergely, T.W. Clyne, Numerical modelling of transient liquid phase bonding and other diffusion controlled phase changes, J. Mater. Sci. 40 (9) (2005) 2505–2511, https://doi.org/10.1007/s10853-005-1983-y.
[45] P.Y. Wen, B. Hu, J.S. Han, H.W. Luo, A strong and ductile medium Mn steel manufactured via ultrafast heating process, Journal of Materials Science & Technology 97 (2022) 54–68, https://doi.org/10.1016/j.jmst.2021.04.035.
[46] W.L. Yu, L.H. Qian, X. Peng, T.L. Wang, K.F. Li, C.Z. Wei, Z.X. Chen, F.C. Zhang, J. Y. Meng, Roles of Al in enhancing the thermal stability of reverted austenite and mechanical properties of a medium-Mn TRIP steel containing 2.7 Mn, Journal of Materials Science & Technology (2023), https://doi.org/10.1016/j.jmst.2023.04.011.
[47] M. Calcagnotto, Y. Adachi, D. Ponge, D. Raabe, Deformation and fracture mechanisms in fine- and ultrafine-grained ferrite/martensite dual-phase steels and the effect of aging, Acta Mater. 59 (2) (2011) 658–670, https://doi.org/10.1016/j.actamat.2010.10.002.
[48] X.C. Xiong, B. Chen, M.X. Huang, J.F. Wang, L. Wang, The effect of morphology on the stability of retained austenite in a quenched and partitioned steel, Scr. Mater. 68 (5) (2013) 321–324, https://doi.org/10.1016/j.scriptamat.2012.11.003.
[49] X.D. Tan, D. Ponge, W.J. Lu, Y.B. Xu, X.L. Yang, X. Rao, D. Wu, D. Raabe, Carbon and strain partitioning in a quenched and partitioned steel containing ferrite, Acta Mater. 165 (2019) 561–576, https://doi.org/10.1016/j.actamat.2018.12.019.
[50] M. Koyama, E. Akiyama, K. Tsuzaki, Hydrogen embrittlement in a Fe–Mn–C ternary twinning-induced plasticity steel, Corros. Sci. 54 (2012) 1–4, https://doi.org/10.1016/j.corsci.2011.09.022.
[51] S. Morito, H. Tanaka, R. Konishi, T. Furuhara, T. Maki, The morphology and crystallography of lath martensite in Fe-C alloys, Acta Mater. 51 (6) (2003) 1789–1799, https://doi.org/10.1016/S1359-6454(02)00577-3.
[52] V.S.A. Challa, X.L. Wan, M.C. Somani, L.P. Karjalainen, R.D.K. Misra, Significance of interplay between austenite stability and deformation mechanisms in governing three-stage work hardening behavior of phase-reversion induced nanograined/ultrafine-grained (NG/UFG) stainless steels with high strength-high ductility combination, Scr. Mater. 86 (2014) 60–63, https://doi.org/10.1016/j.scriptamat.2014.05.010.
[53] J.Y. Li, Y.B. Xu, B. Lu, Y.M. Yu, Y. Jing, W.H. Sun, Improvement of strength-ductility combination in ultra-high-strength medium-Mn Q&P steel by tailoring the characteristics of martensite/retained austenite constituents, J. Mater. Res. Technol. 18 (2022) 352–369, https://doi.org/10.1016/j.jmrt.2022.02.088.
[54] B. Hu, B.B. He, G.J. Cheng, H.W. Yen, M.X. Huang, H.W. Luo, Super-high-strength and formable medium Mn steel manufactured by warm rolling process, Acta Mater. 174 (2019) 131–141, https://doi.org/10.1016/j.actamat.2019.05.043.